

Optimization Design and Control of Single-Stage Single-Phase PV Inverters for MPPT Improvement

Bin Guo , Mei Su, Yao Sun , Member, IEEE, Hui Wang , Bin Liu , Xin Zhang , Senior Member, IEEE, Josep Pou , Fellow, IEEE, Yongheng Yang , Senior Member, IEEE, and Pooya Davari , Senior Member, IEEE

Abstract—Due to the inherent double-frequency ($2f_0$) ripple in single-stage single-phase photovoltaic grid-connected inverters, the maximum power point tracking (MPPT) will inevitably be affected. To improve the MPPT performances, a passive *LC* power decoupling circuit with a robust second-order sliding-mode control (SOSMC) is thus proposed in this article. With the passive *LC* decoupling path, the double-frequency pulsation on the dc link is effectively cancelled out. Thus, the MPPT accuracy is significantly enhanced, and the utilization of a small dc-link capacitor becomes possible. However, resonance between the *LC* circuit and the main dc-link capacitor may appear, which can be damped through an active damping method. Additionally, the proposed SOSMC ensures good steady-state, dynamic performance (voltage fluctuation and settling time), and the robustness of the dc-link voltage, which is also beneficial to MPPT control in terms of high accuracy and fast dynamics. The systematic design of SOSMC is presented, and a detailed parameter optimization design of *LC* decoupling circuit is discussed. Experimental tests are performed on a 2.5-kW single-stage single-phase grid-connected inverter, and the results validate the effectiveness of the proposed strategy.

Index Terms—Double-frequency ripple, maximum power point tracking (MPPT) performance improvement, parameter optimization design, second-order sliding mode control (SOSMC), single-stage single-phase photovoltaic (PV) system.

Manuscript received November 14, 2019; revised March 19, 2020; accepted April 22, 2020. Date of publication April 26, 2020; date of current version July 31, 2020. This work was supported in part by the National Key R&D Program of China under Grant 2018YFB0606005, in part by the National Natural Science Foundation of China under Grant 61873289, in part by the Key R&D Program of Hunan Province under Grant 2019GK2211, in part by the Hunan Provincial Key Laboratory of Power Electronics Equipment and Grid under Grant 2018TP1001, in part by the Project of Innovation-Driven Plan in Central South University under Grant 2019CX003, in part by the Major Project of Changzhutan Self-Dependent Innovation Demonstration Area under Grant 2018XK2002, and in part by the Hunan Provincial Innovation Foundation for Postgraduate under Grant CX20190122. Recommended for publication by Associate Editor C. A. Canesin. (Corresponding author: Yao Sun.)

Bin Guo, Mei Su, Yao Sun, and Hui Wang are with the School of Automation, Central South University, Changsha 410083, China (e-mail: binguo_mail@csu.edu.cn; sumeicsu@mail.csu.edu.cn; yaosuncsu@gmail.com; wanghui9cp9@csu.edu.cn).

Bin Liu is with the School of Electrical Engineering, Guangxi University, Nanning 530004, China (e-mail: bingo.liu@csu.edu.cn).

Xin Zhang was with the School of Electrical and Electronic Engineering, Nanyang Technological University, Singapore 639798, Singapore. He is now with the College of Electrical Engineering, Zhejiang University, Hangzhou 310027, China (e-mail: jackzhang@ntu.edu.sg).

Josep Pou is with the School of Electrical and Electronic Engineering, Nanyang Technological University, Singapore 639798, Singapore (e-mail: josep.pou@ieee.org).

Yongheng Yang and Pooya Davari are with the Department of Energy Technology, Aalborg University, 9100 Aalborg, Denmark (e-mail: yoy@et.aau.dk; pda@et.aau.dk).

Color versions of one or more of the figures in this article are available online at <https://ieeexplore.ieee.org>.

Digital Object Identifier 10.1109/TPEL.2020.2990923

I. INTRODUCTION

NOWDAYS, distributed power generation systems based on renewable energy (solar and wind energy) have received considerable attention due to the increasing electricity demand and depletion of fossil fuels [1], [2]. Owing to the government policies, feed-in-tariff and cost reduction of photovoltaic (PV) installations, PV power generation has also gained considerable popularity in recent years [3].

In general, a typical grid-connected PV system has more than one power-conversion stages [4]. The first stage uses a dc–dc converter to step up the PV voltage, where the maximum power point tracking (MPPT) is implemented. The output power is then inverted using an inverter and fed to the grid [5]. The multistage configurations have advantages, such as flexible control implementation (i.e., the MPPT is achieved in the frontstage; the power feeding-in control is attained in the inverter), whereas the efficiency of the entire system may be low. In contrast, the single-stage PV system employs a single power conversion (i.e., inverter), which performs the following two functions: 1) extracts peak available power from the solar PV arrays by employing a proper MPPT algorithm; and 2) transfers the extracted dc power to the ac grid while meeting power quality requirements [6]. In all, the single-stage conversion is superior over the multistage systems in terms of efficiency, compactness, and cost-effectiveness [7], [8].

For the single-stage single-phase PV system, it is difficult to achieve fast and accurate MPPT due to its single conversion structure. This is because, as seen from the point of view of MPPT, it is desired that the dc-link voltage can be changed quickly, potentially leading to fast MPPT dynamics. However, for the dc-link voltage control, rapid changes in the dc-link voltage may challenge the control stability. Moreover, as shown in Fig. 1, the instantaneous output power is pulsating at twice the line frequency, which is reflected as double-frequency ($2f_0$) ripples with f_0 being the fundamental frequency of the grid on the dc-link voltage. The pulsation then makes the operating point of the PV array away from the desired MPPT condition [9]. This reduces the MPPT accuracy and system efficiency. Hence, the tracking accuracy and also the entire system efficiency are affected. This means that in single-stage single-phase PV systems, the MPPT accuracy and dynamics issue need to be properly addressed.

To eliminate the dc-link $2f_0$ ripples so as to improve the MPPT accuracy, a straightforward way is to use bulky electrolytic capacitors (E-caps) [10] on the dc link so that the voltage pulsation

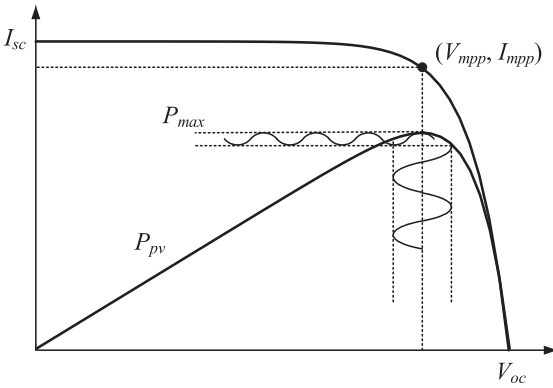


Fig. 1. Illustration of the $2f_0$ components and the impact on the MPPT. I_{sc} is short circuit current, V_{oc} is open-circuit voltage, P_{max} is maximum power, P_{pv} is PV power, and V_{mpp} and I_{mpp} are voltage and current at MPP, respectively.

can be reduced to an acceptable value. However, large E-caps lead to low power density and limited system lifetime [11]. What is more, since the MPPT is realized by regulating the dc-link voltage in single-stage systems, the bulky E-caps with large time constants will lead to slow dynamics of tracking the maximum power point (MPP). An alternative is to use an LC series resonant branch [12] to provide a zero-impedance path for the $2f_0$ -ripple current. By doing so, the requirement of the dc-link capacitor can be significantly reduced. However, the size of the overall system is increased, as the resonant frequency should be $2f_0$. Accordingly, several active power decoupling (APD) methods that utilize auxiliary energy storage elements and power control circuits to buffer the $2f_0$ -ripple power were developed [13]–[16]. With the APD methods, the bulky dc-link E-caps can be replaced by even smaller film capacitors. Yet, when comparing with the LC decoupling solution, the APD methods suffer from complex control and low efficiency, which is not acceptable in PV power generation systems. Furthermore, dedicated control strategies [17]–[19] can be employed in the preceding stage of two-stage inverters to reduce the dc-link capacitance, and the MPPT performance will not be affected. The main idea in these control strategies is to increase the effective impedance of the frontstage seen from the dc link, thus forcing the $2f_0$ power to be buffered by a small dc-link capacitor. Although the above-mentioned methods can improve the performance of single-phase PV systems to a large extent, these active control methods cannot be applied in single-stage inverters. In addition, when the PV voltage is higher than the dc-link voltage, the PV power will be directly transferred, and the inverter operates as a single-stage topology [20]. In this case, the MPPT accuracy is also degraded due to the $2f_0$ -ripples at dc link. To tackle this, a low-frequency harmonic elimination pulselwidth modulation scheme was introduced in [21], where a low $2f_0$ -ripple on Z-source capacitors can be achieved. Additionally, in [22], a new control and modulation strategy was presented to further mitigate the $2f_0$ -ripples. Notably, the above-mentioned methods are specifically for Z-source inverters instead of conventional PV inverters [2].

For the tracking speed of MPP, the prior-art approaches are to enhance the dynamic performance of the dc-link voltage control. For instance, in [23], an adaptive proportional-integral

(PI) control strategy was developed, and with this, a tradeoff between reduction of dc-link voltage fluctuations and grid current harmonics was achieved. However, the bandwidth of the voltage loop must be low enough to suppress the $2f_0$ -ripples. Hence, the improvements presented in [23] are limited. A low-pass filter [24] or moving average filter (MAF) [25] was then used in the voltage control loop to remove the $2f_0$ -ripples. In this cases, the phase lag of filters slows down the response of the entire system. Subsequently, in [26], a second-order notch filter was adopted in the voltage loop to mitigate the $2f_0$ -ripples. Although this can effectively remove the $2f_0$ -ripples and improve the power quality, a phase-crossing of the 180° line was introduced. That is, the improvement is also limited, as a sufficient phase margin of the system should be guaranteed. In [27] and [28], the PI control with an additional feedforward control method was presented to improve the dc-link voltage dynamics. With the two methods, not only the settling time and overshoot of dc-link voltage were improved, but also the coupling between the dc and ac sides was increased. Thus, any noise at input power will be amplified and then induce harmonics at the output; in worst cases, the system stability may be challenged [26].

It should be pointed out that the MPPT accuracy and speed improvement depend on the MPPT algorithm, system design, and control method. From the perspective of the latter, the existing methods are not appropriate in the application of single-stage single-phase PV system to improve MPPT accuracy and speed, meanwhile with high efficiency. Accordingly, this article proposes a design and control method to address the above-mentioned issues. First, a passive LC resonant circuit is employed at the dc link, where the $2f_0$ ripple can be effectively eliminated. In turn, the main dc-link capacitance is reduced, which contributes to improve the MPPT accuracy and system dynamics. Additionally, a voltage control method is proposed to improve the dc-link voltage dynamics and system robustness. More specifically, a robust supertwisting algorithm second-order sliding-mode control (STA-SOSMC) is proposed. Compared with the conventional PI or PI + feedforward control methods, the proposed STA-SOSMC method is better for PV application with the following superiorities.

Fast Dynamic Response: The merits of conventional sliding-mode control (SMC) are maintained, and, thus, the proposed method has fast dynamics, being beneficial to the MPPT.

Strong Robustness: The proposed method is highly robust to system parameter uncertainties (e.g., dc-link capacitance uncertainties) and disturbances (e.g., irradiance variations).

Moreover, the chattering issue, as the main problem of the traditional SMC, is avoided, since the discontinuous input is reduced by enforcing continuous control actions. In addition, an active damping scheme is proposed to mitigate the potential resonance between the LC branch and the dc-link capacitor.

The contributions of this article are summarized as follows.

- 1) A passive LC resonant branch with a detailed analysis and optimal design is proposed to eliminate the $2f_0$ ripples, which benefits to improve the MPPT accuracy and system dynamics.
- 2) A virtual impedance-based active damping method is proposed to alleviate the resonance caused by the LC branch and the main capacitor.

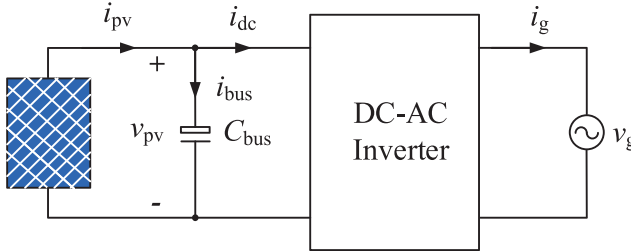


Fig. 2. Configuration of a single-stage single-phase grid-connected PV system.

- 3) The systematic design approach of the STA-SOSMC is presented, and the stability of the entire system is proved by the Lyapunov theory.

The rest of this article is organized as follows. In Section II, the double-frequency issue in single-phase systems is discussed. The proposed optimal design is then detailed in Section III, followed by the control system design and optimization. Experimental tests are performed on a 2.5-kW single-stage single-phase PV inverter, and the results are provided in Section V, where the proposed method is also benchmarked with prior-art solutions. Finally, Section VI concludes this article.

II. MECHANISM OF DOUBLE-FREQUENCY RIPPLE

Fig. 2 shows the general configuration of a single-stage single-phase grid-connected PV inverter, where C_{bus} is the dc-link capacitor, v_g and i_g denote the grid voltage and current, respectively, and v_{pv} and i_{pv} are the PV voltage (dc-link voltage) and current, respectively. Assuming that the grid voltage is purely sinusoidal with the amplitude being V_{gm} and angular frequency being ω_0 , it is expressed as

$$v_g(t) = V_{gm} \sin(\omega_0 t). \quad (1)$$

At unity power factor, the grid current is obtained as

$$i_g(t) = I_{gm} \sin(\omega_0 t) \quad (2)$$

where I_{gm} is the amplitude of the grid current.

According to (1) and (2), the instantaneous power at the ac side is derived as

$$P_{ac}(t) = v_g(t)i_g(t) = \underbrace{\frac{1}{2}V_{gm}I_{gm}}_{\bar{P}} - \underbrace{\frac{1}{2}V_{gm}I_{gm} \cos(2\omega_0 t)}_{\tilde{P}} \quad (3)$$

where \bar{P} is equal to the average input power from the PV array when ignoring the power losses of the inverter, and \tilde{P} is the time varying pulsating power.

In practice, the pulsating power is usually buffered by a passive decoupling capacitor, and the power processed by the dc-link capacitor is shown in Fig. 3. The energy that is being charged or discharged from the capacitor can be calculated as

$$\Delta E = 2 \left(\int_0^{\frac{1}{8f_0}} \tilde{P}(t) dt \right) = \frac{1}{2} C_{bus} (v_{pv(max)}^2 - v_{pv(min)}^2) \quad (4)$$

where $v_{pv(max)}$ and $v_{pv(min)}$ are the maximum and minimum dc-link voltages, respectively.

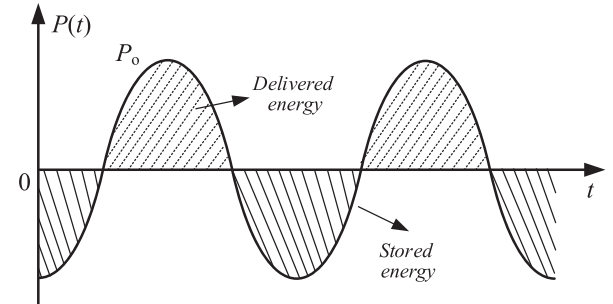


Fig. 3. Total power processed by the dc-link capacitor.

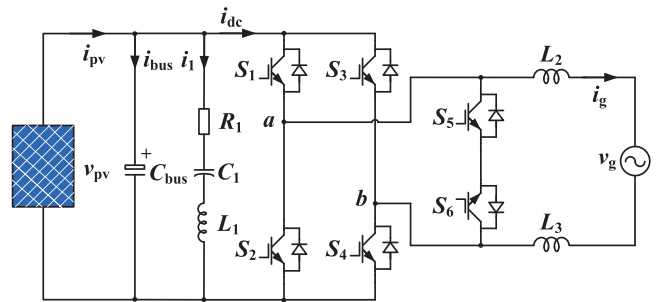


Fig. 4. Topology of a single-stage single-phase PV grid-connected inverter with the LC resonant circuit and an L-type ac filter ($L_2 = L_3$).

According to (4), the voltage ripple on the dc-link capacitor is expressed as

$$\Delta V_{pv} = \frac{V_{gm}I_{gm}}{2\omega_0 C_{bus} V_{pv}} \quad (5)$$

where $V_{pv} = (v_{pv(max)} + v_{pv(min)})/2$ is the average value of the dc-link voltage, and $\Delta V_{pv} = v_{pv(max)} - v_{pv(min)}$. Based on (5), if the voltage ripple is less than 2% of the nominal voltage [16], the minimum dc-link capacitance should be

$$C_{bus} = \frac{V_{gm}I_{gm}}{2\omega_0 V_{pv}^2 2\%}. \quad (6)$$

Accordingly, considering a 2.5-kW single-stage single-phase PV system and assuming that the dc-link voltage varies from 350 to 550 V, the minimum dc-link capacitance is $3248 \mu\text{F}$. This will result in a relatively “bulky” system.

III. DOUBLE-FREQUENCY RIPPLE CANCELLATION AND OPTIMAL DESIGN

As analyzed in Section II, the dc-link voltage ripple can be suppressed by using a large decoupling capacitor. This will, however, increases the tracking time of the MPP in single-stage systems. To deal with this problem, an *LC* resonant circuit is then adopted at the dc link to absorb the pulsating power, as shown in Fig. 4, where C_1 , L_1 , and R_1 denotes the resonant capacitor, inductor, and series equivalent resistance of C_1 and L_1 , respectively, and C_{bus} is the main capacitor. As shown in Fig. 4, a highly efficient and reliable inverter concept (HERIC) is employed as the inverter stage to ensure low leakage currents

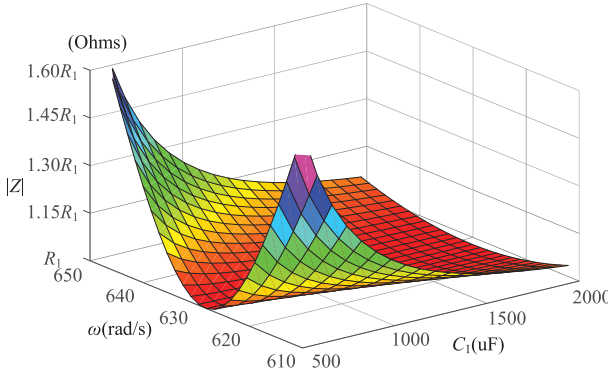


Fig. 5. Series impedance $|Z|$ of the LC branch as a function of angular frequency and resonant capacitance C_1 .

in PV applications [29]. An L -type ($L_2 = L_3$) filter is adopted as the ac-side filter.

A. $2f_0$ -Ripple Cancellation With the LC Decoupling Circuit

The impedance of the LC decoupling circuit is expressed as

$$Z = R_1 + j \left(\omega L_1 - \frac{1}{\omega C_1} \right) \quad (7)$$

where ω is the angular frequency. Clearly, at the frequency of $2f_0$, the capacitive and inductive reactance should be equal to provide a minimum-impedance path for the ripple current. Then

$$Z|_{\omega=\omega_r} = R_1 + j \left(\omega_r L_1 - \frac{1}{\omega_r C_1} \right) = R_1 \quad (8)$$

with

$$\omega_r = 1/\sqrt{L_1 C_1} = 4\pi f_0. \quad (9)$$

As shown in (8), due to the series equivalent resistance R_1 , the LC branch impedance at $2f_0$ is not zero. Thus, the dc-link ripples cannot be fully eliminated. To reduce the $2f_0$ -ripple to a desired value, the maximum value of R_1 is calculated as

$$\frac{R_1(1/\omega_r C_{\text{bus}})}{R_1 + (1/\omega_r C_{\text{bus}})} \Delta i_1 \leq \Delta V_{\text{pv}} \Rightarrow R_1 \leq \frac{\Delta V_{\text{pv}}}{\Delta i_1 - \Delta V_{\text{pv}} \omega_r C_{\text{bus}}} \quad (10)$$

in which $\Delta i_1 = V_{gm} I_{gm} / V_{\text{pv}}$ and ΔV_{pv} are the $2f_0$ -ripple current and $2f_0$ -ripple voltage at the dc link, respectively.

Considering the grid fundamental frequency variation of ± 1 Hz, to effectively reduce the $2f_0$ -ripple, the impedance of the LC branch should be constrained as

$$|Z| = \sqrt{R_1^2 + \left(\frac{\omega}{\omega_r^2 C_1} - \frac{1}{\omega C_1} \right)^2} \leq \sqrt{2} R_1. \quad (11)$$

Fig. 5 shows the impedance with respect to the angular frequency ω and resonant capacitance C_1 . It can be seen in Fig. 5 that the tuning sharpness is dependent on C_1 , and a large capacitor leads to an increased filter passband.

Based on the above-mentioned analysis, it can be concluded that to eliminate the dc-link $2f_0$ -ripple voltages, the series equivalent resistance R_1 of the LC branch should be designed as small as possible. However, small resistance will increase the

volume and cost of the inductor. Moreover, in the case of the grid frequency variation, the selection of inductance and capacitance values involves the robustness, size, cost, and weight of the entire system. Therefore, the design of the LC resonant circuit is an optimization problem.

B. Optimal Design of the LC Decoupling Circuit

For simplicity, this article only takes the volume of the LC decoupling circuit as the optimization objective, since it is an importance factor of the entire system.

1) Inductor and Capacitor Volume Calculation: The volume of the inductor L_1 can be determined considering the following expressions [30], [31]:

$$\left\{ \begin{array}{l} VL_L = K_{\text{vol}} A_p^{0.75} \\ A_p = \frac{P_t \cdot (10^4)}{K_f K_u B_{\text{ac}} J f} \\ J = \frac{I_{1(\text{rms})}}{A_w} \\ R_L = \frac{(MLT)^N}{A_w} \rho \cdot (10^2) \\ N = \sqrt{\frac{L_1 \cdot (10^9)}{A_L}} \\ P_t = U_{L(rms)} I_{1(rms)} = \omega_r L_1 I_{1(rms)}^2 \end{array} \right. \quad (12)$$

where K_{vol} is a constant related to the core material. In this article, the Kool M μ powder core produced by Magnetics Inc. is selected, and K_{vol} is equal to 13.1. Furthermore, in (12), A_p is the area product, P_t is the apparent power of the inductor, K_f is a constant related to the wave shape, which is 4.44 for a sine wave, K_u is the window utilization factor ($K_u = 0.4$ for general application), B_{ac} is the maximum magnetic flux, J and A_w are the current density and cross area of the wire, respectively, $\rho = 1.75 \times 10^{-8} \Omega/\text{m}$ is the resistivity of copper, MLT is the mean length of turn, R_L is the inductor winding resistance, N is the number of turns, and A_L is the inductance factor.

It should be noted that for a specific core, the parameters, for e.g., B_{ac} , MLT , and A_L are determined. However, the optimization design of the inductor needs several iterations and verifications. The flowchart and detailed explanation of the core selection and inductor design will be detailed in Section III-B4. Assuming that a specific core is selected, substituting B_{ac} , MLT , and A_L into (12) gives the inductance volume VL_L as

$$VL_L = k_L \frac{L_1^{9/8}}{R_L^{3/4}} \quad (13)$$

where k_L is a proportional coefficient related to the core parameters. It is expressed as

$$k_L = K_{\text{vol}} \left(\frac{\omega_r (MLT) \rho I_{1(\text{rms})} \cdot (10^{21/2})}{K_f K_u B_{\text{ac}} f A_L^{1/2}} \right)^{3/4}. \quad (14)$$

Regarding the capacitor C_1 , film and/or ceramic capacitors have the disadvantages of high costs as many capacitors are required at the dc link [32]. Thus, E-caps are usually selected. Generally, the volume of the E-caps can be expressed as [33]

$$VL_C = k_C C_1 V^*{}^2 \quad (15)$$

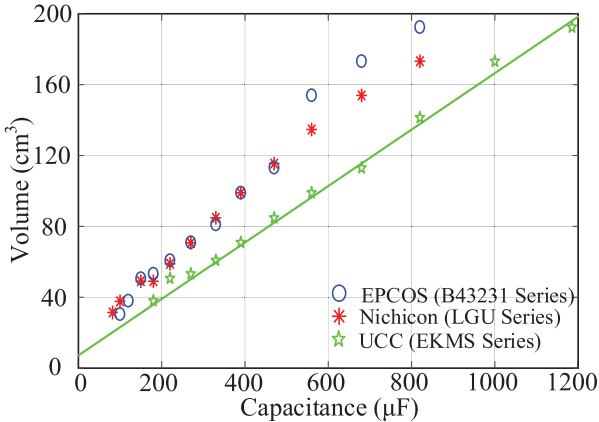


Fig. 6. Volume of the E-caps versus the capacitance from various manufacturer datasheets [35]–[37].

where k_C is the coefficient describing the linear relationship, and V^* is the rated capacitor voltage.

Since the dc-link voltage varies from 350 to 550 V in the single-stage system under study, series and parallel connection of capacitors is usually required. Thus, to ensure enough safety margins, the capacitors with a 315 V rated voltage are selected. According to (15), the volume is proportional to the capacitance value. Fig. 6 shows the E-caps volume versus the capacitance for different capacitors from several manufacturers [34]–[36]. From Fig. 6, it can be seen that for the same capacitance, the capacitors produced by United Chemi-Con (UCC) have the smallest volume. Therefore, the 315 V EKMS-series E-caps from UCC are adopted.

To calculate the volume of the capacitance C_1 , the curve fitting method is adopted. The volume of the capacitance C_1 (VL_C) is expressed as follows:

$$VL_C = a \cdot C_1 + b \quad (16)$$

where a and b are known constants. For simplicity, the impact of the installation and other factors on the volume is not considered. Thus, the total volume of the LC decoupling circuit is expressed as

$$VL_{CL} = VL_L + VL_C. \quad (17)$$

The equivalent resistance of the capacitor includes an ohmic term due to metallization, end-spraying, connections, and a resistance representing the dielectric material. Then

$$R_C = R_\Omega + \frac{\tan \delta}{C_1 \omega} \quad (18)$$

where $\tan \delta$ is the dielectric loss angle. For the selected capacitors, $\tan \delta$ is 0.15. Since the dielectric-related resistance dominates in the low frequency range, whereas ohmic resistance dominates in the higher frequencies [37], the equivalent resistance of the capacitance C_1 at the ripple frequency of $2f_0$ is simplified as $R_c = \tan \delta / C_1 \omega_r$.

2) *Optimization Objective*: According to the above-mentioned analysis, to improve the $2f_0$ -ripple suppression effect, an optimization problem to minimize the volume of the

LC decoupling circuit is formulated as

$$\text{Min } VL_{CL} \quad (19)$$

which is subjected to

$$\begin{cases} \omega_r = 1/\sqrt{L_1 C_1} \\ 0 \leq R_1 \leq \frac{\Delta V_{pv}}{\Delta i_1 - \Delta V_{pv} \omega_r C_{bus}}, \quad R_1 = R_L + R_C \\ |Z| = \sqrt{R_1^2 + (\frac{\omega}{\omega_r^2 C_1} - \frac{1}{\omega C_1})^2} \leq \sqrt{2} R_1, \quad \omega \in [\omega_L, \omega_H] \end{cases} \quad (20)$$

where the desired maximum ripple ΔV_{pv} of the dc link is 4 V, and the angular frequency ω_L and ω_H are 196π and 204π rad/s, respectively. The value of the main capacitor C_{bus} is selected as $200 \mu\text{F}$ to buffer the mismatch power between the input and output power in the case of sudden irradiance changes and to eliminate high-frequency ripple.

3) *Particle Swarm Optimization Algorithm*: As shown in (19) and (20), the inductor optimization design problem is nonlinear, constrained, and nonconvex. Thus, the general method based on the gradient optimization algorithm is not easy to solve this problem. To tackle this issue, the intelligent optimization algorithms are considered. Compared with the artificial bee colony, simulated annealing, genetic algorithm, and artificial neural network optimization algorithms, the particle swarm optimization (PSO) algorithm has the advantages of easy implementation, fast calculation capability, and the ability to determine the extreme value irrespective of external conditions. Thus, the PSO algorithm is adopted in this article to obtain the optimal parameters of the LC decoupling circuit. In the PSO algorithm, each particle represents a possible solution. In a D -dimensional vector, the current position of the i th particle is $X_i = (x_{i1}, \dots, x_{id})$, and the current velocity is $V_i = (v_{i1}, \dots, v_{id})$. To determine the best behavior of particles, let $f(X) = VL_{CL}$ be the fitness function. The velocity and position of the i th particle in the D -dimensional space are updated as [38]

$$\begin{aligned} v_{id}(k+1) &= w v_{id}(k) + c_1 r_1 (P\text{best}_{id}(k) - x_{id}(k)) \\ &\quad + c_2 r_2 (G\text{best}_d(k) - x_{id}(k)) \end{aligned} \quad (21)$$

$$x_{id}(k+1) = x_{id}(k) + v_{id}(k+1) \quad (22)$$

where $i = 1, 2, \dots, n$, n is the number of particles. $d = 1, 2, \dots, D$; and k is the iteration number. $P\text{best}_i$ is the personal best experience that the i th particle has experienced, and $G\text{best}$ is the best position in the swarm found so far. w is the inertia weight, c_1 and c_2 are the cognitive and social acceleration constant, respectively, and r_1 and r_2 are random numbers between 0 and 1.

A large inertia weight w can improve the global search capability at the early iteration stage, whereas a relatively small inertia weight is helpful for fast convergence. Thus, to achieve a balance between local and global search abilities, a time-varying inertia weight is adopted in the optimization, which is shown as

$$w = (w_{\max} - w_{\min}) \frac{K - k}{K} + w_{\min} \quad (23)$$

in which K and k are the maximum and current iteration number, respectively, and w_{\max} and w_{\min} are the maximum and minimum inertia weights that are set as 0.9 and 0.4, respectively.

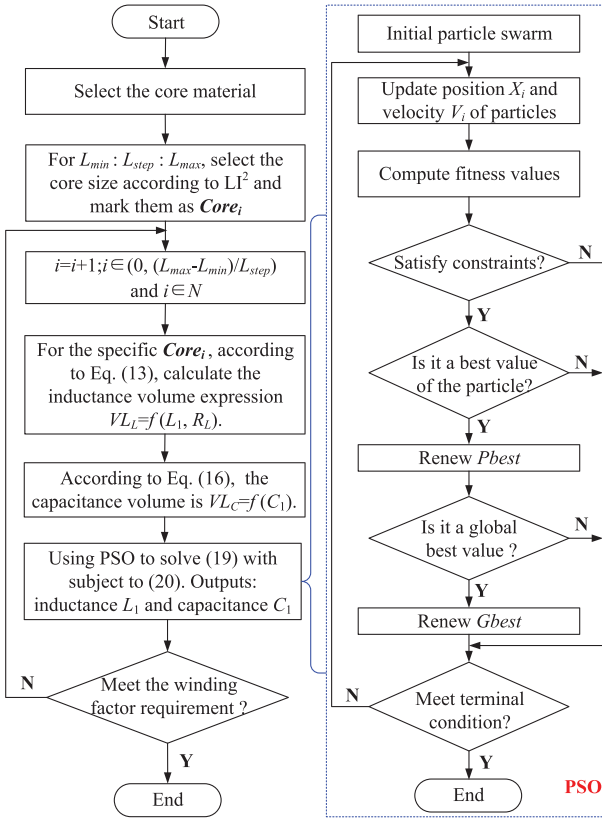


Fig. 7. Flowchart of the optimization for the core selection, inductor, and capacitor design.

Similarly, time-varying acceleration constants c_1 and c_2 can be adopted as

$$\begin{cases} c_1 = (c_{1\max} - c_{1\min}) \frac{K-k}{K} + c_{1\min} \\ c_2 = (c_{2\max} - c_{2\min}) \frac{K-k}{K} + c_{2\min} \end{cases} \quad (24)$$

where $c_{1\max}$, $c_{2\max}$ and $c_{1\min}$, $c_{2\min}$ are the maximum and minimum acceleration constants, respectively. In this article, $c_{1\max}$ and $c_{2\max}$ are equal to 2.5, and $c_{1\min}$ and $c_{2\min}$ are equal to 0.5.

4) *PSO-Based Optimal Design of the LC Circuit*: In this article, for the specific optimization, the capacitance C_1 and inductance L_1 are chosen as the variables $X_i = (C_1, L_1)$ to optimize. Thus, the space dimension D is 2. According to the optimization objective in (19), the corresponding fitness function is defined as $f(X) = VL_{CL}$. The constraints are shown in (20). $P_{\text{best},i} = (P_{\text{best},1}, P_{\text{best},2})$ is the best position that the i th particle has experienced, and $G_{\text{best}} = (G_{\text{best},1}, G_{\text{best},2})$ is the best position that all the particles have experienced. When the optimization meets the terminal conditions, the position of G_{best} is the desired value of L_1 and C_1 , and its fitness value $f(X)$ is the minimum volume of the LC resonant circuit.

The overall flowchart for the inductor and capacitor optimal design based on the PSO is shown in Fig. 7, where L_{\min} and L_{\max} are the minimum and maximum inductance values that are set to 0.1 and 5 mH, respectively; L_{step} is the optimization step size; and $L_{\text{step}} = 0.1$ mH. Before explaining in detail how the inductor

L_1 and capacitor C_1 are designed, the working principle of the PSO algorithm is provided as follow [39].

- Step 1) Initialize a group of particles while satisfying the constraints. Then, calculate the fitness of the initial particles.
- Step 2) Update position X_i and velocity V_i of particles.
- Step 3) Calculate the new fitness of the updated particles.
- Step 4) Check whether the updated particles still satisfy the constraints, if not, go to Step 6).
- Step 5) Update P_{best} and G_{best} .
- Step 6) Check if the terminal condition is met. The terminal condition is defined as satisfying maximum iteration steps and fitness value. If not, go to Step 2).

According to Fig. 7, the detailed design steps of inductor L_1 and capacitor C_1 are explained as follow. For $L_{\min} : L_{\text{step}} : L_{\max}$, the core size is selected according to LI^2 , where L is inductance value, and I is the current value. These cores are then marked as core_i , where $i \in (0, (L_{\max} - L_{\min})/L_{\text{step}})$. As mentioned previously, the Kool M μ powder core is selected in this article, and the parameters of different cores can be stored as a database in MATLAB. Thus, when a specific core is selected, e.g., core_i is selected, the parameters, such as B_{ac} , MLT, and A_L , can be obtained through the database. Then, according to (13) and (14), the expression of VL_L corresponding to L_1 can be determined. Eventually, VL_{CL} corresponding to L_1 and C_1 is known. As a result, with the PSO algorithm, a set of parameters L_1 and C_1 and the minimum volume VL_{CL} are obtained for the specific core, core_i . However, although the inductance L_1 is determined, the winding factor of the inductor may not meet the requirement. Then, the core size is changed to core_{i+1} , and the above-mentioned steps are repeated until the winding factor requirement is met. Since the core size is selected from small to large, when core_{i+1} is selected and if its winding factor meets the design requirement, it can be considered that the winding factor reaches its optimal value at this moment.

Fig. 8 shows the evolutionary process and final optimization results of the inductor L_1 and capacitor C_1 . From Fig. 8, it can be seen that the volume of the LC decoupling circuit is minimized when the inductance and capacitance are 1.865 mH and 1358 μ F, respectively. However, since the commercially available capacitors are discrete, in this article, the inductance and capacitance are then selected as 1.81 mH and 1400 μ F, respectively. The series equivalent resistance R_1 is obtained as 0.265 Ω in the design.

IV. CONTROL DESIGN

As described in Section III, with the passive LC decoupling circuit, the main dc-link capacitance C_{bus} is substantially reduced, and, therefore, the dynamics of the system can be significantly enhanced. However, due to the LC resonant circuit, it is easy to result in oscillatory peaks and transient [40], [41]. To address this issue, an improved damping scheme and a robust SOSMC method are proposed in this section to realize dc-link voltage dynamic performance improvement. As a result, the MPP tracking speed is further improved.

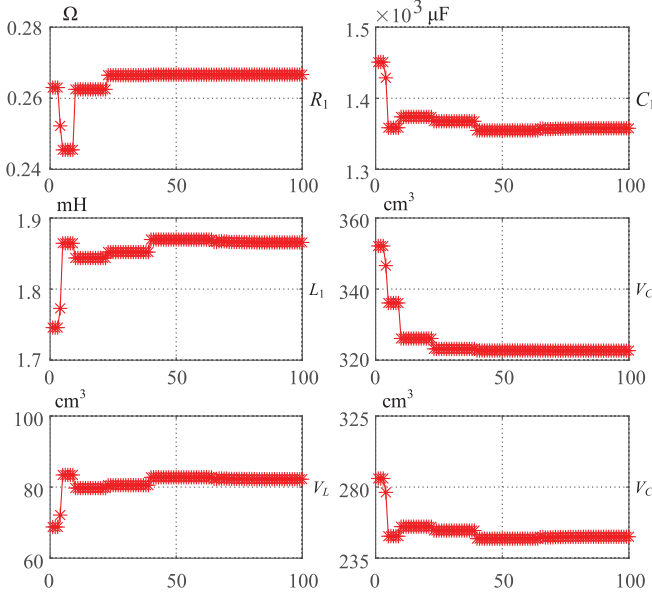


Fig. 8. Evolutionary process and optimall results with the PSO algorithm.

A. System Modeling

As shown in Fig. 4, the single-stage single-phase grid-connected inverter can be described as

$$C_{\text{bus}} \frac{dv_{\text{pv}}}{dt} = i_{\text{pv}} - i_1 - i_{\text{dc}} \quad (25)$$

$$C_1 \frac{dv_1}{dt} = i_1 \quad (26)$$

$$L_1 \frac{di_1}{dt} = v_{\text{pv}} - v_1 - i_1 R_1 \quad (27)$$

$$L_g \frac{di_g}{dt} = u_{ab} - v_g \quad (28)$$

where $L_g = L_2 + L_3$, i_{dc} is the dc-link output current, v_1 is the voltage of the capacitor C_1 , i_1 is the LC branch current, and u_{ab} is the inverter output voltage.

B. Dynamic Characteristic Analysis of the LC Circuit

According to (25)–(27), the transfer function $G_p(s)$ from the dc-link current to the PV voltage is derived as

$$\begin{aligned} G_p(s) &= \left. \frac{v_{\text{pv}}(s)}{-i_{\text{dc}}(s)} \right|_{i_{\text{pv}}(s)=0} \\ &= \frac{C_1 L_1 s^2 + R_1 C_1 s + 1}{C_{\text{bus}} C_1 L_1 s^3 + R_1 C_{\text{bus}} C_1 s^2 + (C_{\text{bus}} + C_1)} \end{aligned} \quad (29)$$

which indicates that the system is underdamped when the resistance R_1 is small. In other words, the system is prone to instability. Clearly, an intuitive way to enhance the stability is to increase the resistance of the LC circuit. The Bode diagram of $G_p(s)$ with different values of R_1 is shown in Fig. 9. Yet, as aforementioned, increasing the resistance will reduce the tuning sharpness and increase the system losses. Therefore, it is more attractive to solve this issue by using active damping schemes.

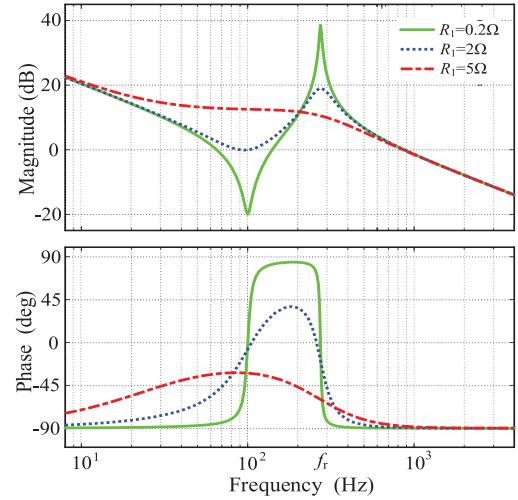
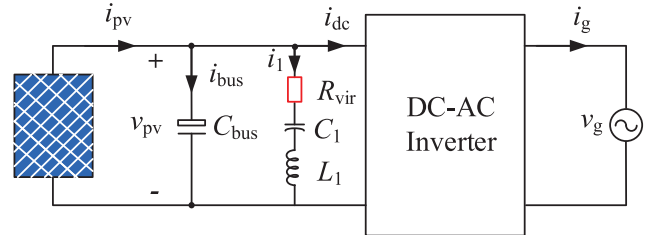
Fig. 9. Bode diagram of the transfer function $G_p(s)$ with different series resistances R_1 .

Fig. 10. System configuration of the single-stage single-phase PV inverter with the proposed virtual resistance.

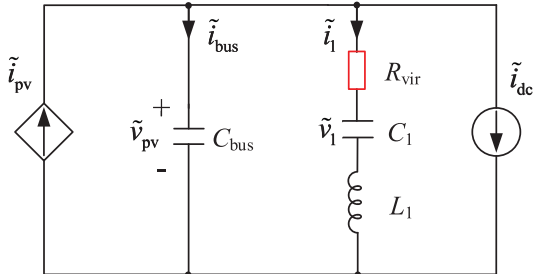


Fig. 11. Small-signal equivalent circuit of the inverter system shown in Fig. 10 with the virtual resistance.

C. Proposed Active Damping Scheme

A virtual resistance-based active damping scheme, shown in Fig. 10, is then proposed in this section. With the state-space averaging approach, the small-signal equivalent circuit of the system with the virtual resistance is given in Fig. 11. Supposing that the dc-link voltage v_{pv} can track its reference well, the dynamics of the voltage and current loops can then be neglected. Accordingly, the small-signal block diagram to realize the virtual resistance is obtained, as shown in Fig. 12, which indicates that the voltage reference of dc link should be

$$v_{\text{pv}}^{**} = v_{\text{pv}}^* - R_{\text{vir}}(i_1 - i_1^*) = v_{\text{pv}}^* - R_{\text{vir}}\tilde{i}_1 \quad (30)$$

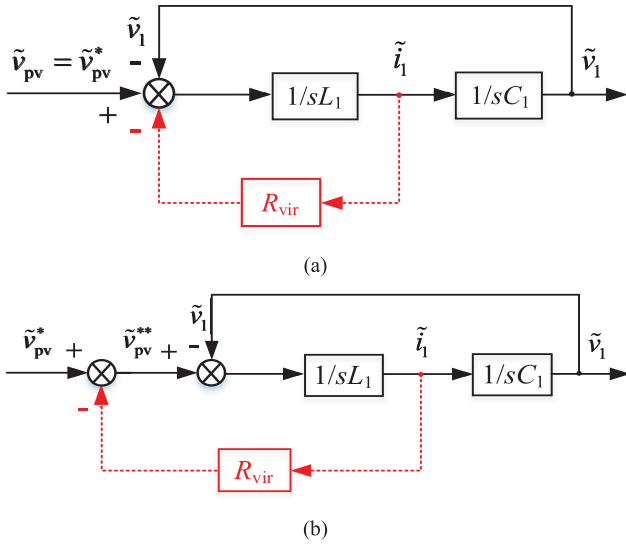


Fig. 12. Realization of the virtual resistance. (a) Original control block diagram. (b) Equivalent transformation.

where v_{pv}^* is the voltage reference from the MPPT, i_1^* and \tilde{i}_1 represent the steady-state value and small-signal value of i_1 , respectively, and R_{vir} is the total resistance (the sum of virtual resistance and the series equivalent resistance R_1).

Since the $2f_0$ -pulsating power is absorbed by the proposed LC decoupling circuit, i_1^* will be nearly sinusoidal with $2f_0$ -components. Thus, to realize (30) in practice, a notch filter with the central frequency being $2f_0$ is used. The transfer function of the notch filter is expressed as

$$G_{\text{notch}}(s) = \frac{s^2 + \omega_n^2}{s^2 + 2\zeta\omega_n s + \omega_n^2} \quad (31)$$

where $\omega_n = 4\pi f_0$, and ζ is the damping ratio of the notch filter. Consequently, (30) is modified as

$$v_{pv}^{**} = v_{pv}^* - R_{vir} i_1 G_{\text{notch}}(s). \quad (32)$$

D. Design of the SOSMC for the Voltage Loop

Generally, the control of the grid-connected PV inverter consists of two loops: an outer voltage loop and an inner current loop. To achieve zero steady-state error tracking of the current, a proportional multiresonant (P+MR) controller is adopted in the current loop. Due to the limited space, the analysis and design of the inner current loop are not discussed in this article, which can be referred to [42]. As in single-stage systems, the MPPT is achieved by regulating the dc-link voltage. The control objectives of the voltage loop are the following:

- 1) low voltage fluctuation and small settling time;
- 2) zero steady-state error;
- 3) strong robustness.

After the $2f_0$ -ripple is eliminated by the LC circuit, these objectives can be achieved by a properly designed SOSMC, as detailed in the following.

1) Sliding Surface of the SOSMC: Rewriting (25) as

$$C_{\text{bus}} \frac{dv_{pv}}{dt} = \frac{1}{v_{pv}} (P_{\text{in}} - P_o - P_{lc}) \quad (33)$$

where $P_{\text{in}} = v_{pv} i_{pv}$ is the PV input power, P_{lc} is the power absorbed by the LC circuit, and $P_o = v_{pv} i_{dc}$.

Supposing that the grid current tracks its reference well, (33) is rewritten as

$$\frac{dz}{dt} = \frac{1}{C_{\text{bus}}} (P_{\text{in}} - P^*) \quad (34)$$

with $z = v_{pv}^2/2$, $P^* = P_o + P_{lc} = V_{gm} I_{gm}^*/2$, and I_{gm}^* being the grid current reference.

Since the control objective of the SOSMC is to regulate the dc-link voltage, and to add a degree of freedom to adjust the voltage loop bandwidth, a voltage error integral term is included as a state variable. Therefore, the sliding surface is defined as

$$s = x_1 + \lambda x_2 \quad (35)$$

in which $x_1 = z - z^*$, $z^* = (v_{pv}^*)^2/2$, $x_2 = \int x_1 dt$, and λ is a positive sliding coefficient.

2) Control Law Design: The supertwisting algorithm, which has the advantage of finite-time convergence to the set point and rejecting smooth disturbances of arbitrary shapes, has been developed for the system with the relative degree-1 [43].

In the dual-loop control, the voltage loop gives the current amplitude reference. Thus, the amplitude of the grid current reference I_{gm}^* can be regarded as the control input of (34). To control the dc-link voltage, the global control law I_{gm}^* is made up of two terms: the equivalent control term $I_{gm(eq)}^*$ and the supertwisting control term $I_{gm(st)}^*$. Thus, the global control law is defined as

$$I_{gm}^* = I_{gm(eq)}^* + I_{gm(st)}^* \quad (36)$$

where the equivalent control term $I_{gm(eq)}^*$ can be obtained by solving the following equation:

$$\dot{s} = 0. \quad (37)$$

Considering that $z^* = (v_{pv}^*)^2/2$, which is from the MPPT algorithm, is a slow-time-varying variable. Thus, its derivative can be viewed as zero. Substituting (34) and (35) into (37), $I_{gm(eq)}^*$ is obtained as

$$I_{gm(eq)}^* = \frac{2C_{\text{bus}}}{V_{gm}} \left(\frac{P_{\text{in}}}{C_{\text{bus}}} + \lambda x_1 \right). \quad (38)$$

The supertwisting term $I_{gm(st)}^*$ is given as

$$I_{gm(st)}^* = -\frac{2C_{\text{bus}}}{V_{gm}} u_{st} \quad (39)$$

where u_{st} takes the following form [43]:

$$u_{st} = -\alpha_1 |s|^{1/2} \text{sign}(s) + v \\ v = -\alpha_2 \text{sign}(s) \quad (40)$$

with α_1 and α_2 being positive constants.

Substituting (38) and (39) into (36), the amplitude of grid current reference is expressed as

$$I_{gm}^* = \underbrace{\frac{2P_{in}}{V_{gm}} + \frac{2C_{bus}}{V_{gm}}\lambda x_1}_{I_{gm(eq)}^*} + \underbrace{\frac{2C_{bus}}{V_{gm}}(\alpha_1|s|^{1/2}\text{sign}(s) + \alpha_2 \int_0^t \text{sign}(s)d\tau)}_{I_{gm(st)}^*}. \quad (41)$$

From close inspection of (41), it can be seen that the equivalent control term $I_{gm(eq)}^*$ in (41) can be regarded as a proportional (P) controller with the power feedforward in traditional PI with the feedforward control strategy. In the proposed STA-SOSMC, the equivalent control term is to deal with the known system dynamics, and the supertwisting control term is to address the issues due to uncertainties from parameter errors and unmodeled dynamics.

3) Model Uncertainty and Robustness: Considering the tolerance of the capacitor C_{bus} , the power losses of the inverter, and any other external disturbances, (34) is rewritten as

$$\frac{dz}{dt} = \frac{1}{\hat{C}_{bus}}(P_{in} - P^*) + \frac{\Delta C_{bus}}{\hat{C}_{bus}C_{bus}}(P_{in} - P^*) + \zeta \quad (42)$$

where ζ includes the power losses and any other disturbances, and \hat{C}_{bus} is the nominal value of C_{bus} that is given as

$$\hat{C}_{bus} = C_{bus} + \Delta C_{bus} \quad (43)$$

with ΔC_{bus} denoting the parameter error. Equation (34) can then be further rewritten as

$$\frac{dz}{dt} = \frac{1}{\hat{C}_{bus}}(P_{in} - P^*) + d = \frac{d\hat{z}}{dt} + d \quad (44)$$

in which \hat{z} is the nominal value of z , and d is the total disturbance that is given as

$$d = \frac{\Delta C_{bus}}{\hat{C}_{bus}C_{bus}}(P_{in} - P^*) + \zeta. \quad (45)$$

Taking into account the physical limitation of the system in practice and its behavior during the operation, it is assumed that the perturbation is bounded such as

$$|d| < \delta \quad (46)$$

where δ is a known positive constant.

4) Stability Analysis: According to (35) and (44), the first-order derivative of the sliding variable s is derived as

$$\dot{s} = \dot{x}_1 + \lambda x_1 = \dot{\hat{x}}_1 + \lambda x_1 + d \quad (47)$$

where \hat{x}_1 is the nominal value of x_1 . Substituting (41) into (47), the closed-loop system is derived as

$$\begin{aligned} \dot{s} &= -\alpha_1|s|^{1/2}\text{sign}(s) + v + d \\ v &= -\alpha_2\text{sign}(s). \end{aligned} \quad (48)$$

To prove the stability of the system, the Lyapunov function is chosen as [44]

$$\begin{aligned} V &= 2\alpha_2|s| + \frac{1}{2}v^2 + \frac{1}{2}(\alpha_1|s|^{1/2}\text{sign}(s) - v)^2 \\ &= \zeta^T P \zeta \end{aligned} \quad (49)$$

with

$$\begin{aligned} \zeta^T &= [|s|^{1/2}\text{sign}(s) \quad v] \\ P &= \frac{1}{2} \begin{bmatrix} 4\alpha_2 + \alpha_1^2 & -\alpha_1 \\ -\alpha_1 & 2 \end{bmatrix}. \end{aligned}$$

Its time derivative is then obtained as

$$\dot{V} = -\frac{1}{|s|^{1/2}}\zeta^T Q \zeta + \frac{d}{|s|^{1/2}}q^T \zeta \quad (50)$$

where

$$\begin{aligned} Q &= \frac{\alpha_1}{2} \begin{bmatrix} 2\alpha_2 + \alpha_1^2 & -\alpha_1 \\ -\alpha_1 & 1 \end{bmatrix} \\ q^T &= \left[\left(2\alpha_2 + \frac{\alpha_1^2}{2} \right) \quad \frac{-\alpha_1}{2} \right]. \end{aligned}$$

Applying the bounds $|d| < \delta$, as demonstrated in [44], it can be obtained that

$$\dot{V} \leq -\frac{1}{|s|^{1/2}}\zeta^T \tilde{Q} \zeta \quad (51)$$

with

$$\tilde{Q} = \frac{\alpha_1}{2} \begin{bmatrix} 2\alpha_2 + \alpha_1^2 - (\frac{4\alpha_2}{\alpha_1} + \alpha_1)\delta & -(\alpha_1 + 2\delta) \\ -(\alpha_1 + 2\delta) & 1 \end{bmatrix}.$$

Obviously, \dot{V} is negative if $\tilde{Q} > 0$, which represents that the system is globally asymptotically stable if the gains satisfy

$$\begin{cases} \alpha_1 > 2\delta \\ \alpha_2 > \alpha_1 \frac{5\alpha_1\delta + 4\delta^2}{2(\alpha_1 - 2\delta)} \end{cases} \quad (52)$$

When the sliding mode occurs on the sliding surface, $s=0$ and $\dot{s}=0$ are guaranteed. Thus, according to (35), the dynamic behavior of the dc-link voltage is described as

$$x_1(t) = x_1(0)e^{-\lambda t}. \quad (53)$$

It is clear that the tracking error converges to zero exponentially. Therefore, the sliding coefficient λ can be regarded as a degree of freedom to adjust the system bandwidth.

5) Parameter Selection: Three parameters for SOSMC, i.e., λ , α_1 , and α_2 , should be properly designed to ensure the dynamics and stability of the system. According to (53), λ denotes the pole of sliding-mode dynamics. Thus, for the controller, it will be beneficial to select λ as large as possible, but at the cost of the tracking performance. If λ is too large, it can cause large overshoots, whereas a controller with small λ leads to longer tracking time and slower error convergence.

Note that in the single-stage single-phase PV system, the dc-link voltage reference is provided by the MPPT algorithm.

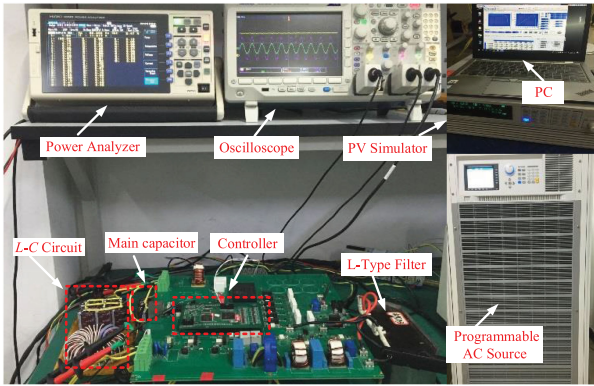


Fig. 13. Experimental setup of the single-stage single-phase PV system.

Therefore, to ensure the speed of the MPPT and the entire system stability, the following two constraints should be taken into account when selecting the parameter λ .

- 1) The minimum setting time t_{\min} of the outer loop should be ten times larger than that of the inner loop [23].
- 2) The maximum setting time t_{\max} of the outer loop should be smaller than the update time of the MPPT algorithm.

Regarding parameters α_1 and α_2 , the inequality (52) must be satisfied to ensure the sliding variable converges to zero in finite time. However, when one sampling computation delay is considered in the digital control system, α_1 and α_2 should be selected more conservative to ensure the system stability. Due to the limited space, the detailed stability discussion of the system with time delays is not considered in this article, which can be referred to [45].

V. EXPERIMENTAL RESULTS

To verify the effectiveness of the proposed method in MPPT accuracy and speed enhancement, experimental tests are performed on a 2.5-kW single-stage single-phase PV grid-connected prototype, as shown in Fig. 13. The control algorithms are implemented in a digital signal processor (DSP TSM320F28335), and the driver signals of insulated gate bipolar transistor (IGBT) are generated by a field programmable gate array (FPGA). The key parameters of the prototype and controller are listed in Table I, and the control block diagram of the voltage loop with the proposed SOSMC strategy is detailed in Fig. 14. A Chroma PV simulator and programmable ac source are adopted to emulate the PV array and grid, respectively. In this article, a perturb and observe (P&O) MPPT algorithm is employed with the updating time of 200 ms. In order to make a tradeoff between the tracking speed and the steady-state oscillations, a variable step size is chosen for the MPPT control. The maximum step size is 6 V and the minimum one is 1 V.

A. Effectiveness of the Proposed $2f_0$ -Ripple Cancellation Method

Fig. 15 shows the experimental waveforms of the dc-link voltage, grid current, and grid voltage with the proposed method.

TABLE I
EXPERIMENTAL PARAMETERS

Parameters	Values
Power output at MPP: P_{MPP}	2.5 kW
Resonant inductance: L_1	1.81 mH
Resonant capacitance: C_1	1400 μF
Main capacitance: C_{bus}	200 μF
MPPT update time: t_{MPPT}	200 ms
Grid voltage: v_g (rms)	220 V
Grid frequency: f_0	50 Hz
Switching frequency: f_{sw}	20 kHz
Sampling frequency: f_s	40 kHz
Grid-side filter inductance: L_g	2 mH
Virtual resistance: R_{vir}	1.5 Ω
Damping ratio of notch filter: ζ	0.6
SOSMC parameter 1: λ	85
SOSMC parameter 2: α_1	5180
SOSMC parameter 3: α_2	2.0733×10^6

It can be observed in Fig. 15 that the dc-link voltage ripple is 4 V, which is consistent with the theoretical analysis. Therefore, the effectiveness of the LC resonant circuit on the $2f_0$ -ripple cancellation is verified. Furthermore, owing to the small voltage ripple, the steady-state performance of the MPPT is almost not degraded. The static average MPPT efficiency obtained from the PV simulator is 99.5%, which shows a very good tracking accuracy in single-stage PV systems.

To further demonstrate the effectiveness of the proposed $2f_0$ -ripple cancellation strategy, another experiment is carried out, where the grid voltage frequency is suddenly changed from 50 to 49 Hz. The experimental results are shown in Fig. 16. It can be seen in Fig. 16 that the dc-link voltage ripple is slightly increased by 1 V in the case of the 1-Hz change in the grid voltage frequency, indicating that the proposed $2f_0$ -ripple cancellation method is effective.

B. Steady-State Performance Under Grid Voltage Distortions

Fig. 17(a) shows the steady-state waveforms of the dc-link voltage, grid voltage, and grid current with the proposed SOSMC method, where the grid voltage is distorted with the total harmonic distortion (THD) being 3.71%. Fig. 17(b) shows the spectrum of the resultant grid current under the above-mentioned condition. As it is observed in Fig. 17, despite the highly distorted grid voltage, the THD level of the resultant grid current is 2.59%, which is below the standard limit (e.g., 5%).

C. Dynamic Performance of the PV System

To test the dynamic performance of the voltage loop with the proposed SOSMC method, the MPPT algorithm is shielded and the dc-link voltage is controlled as a constant value. Fig. 18(a) and (b) shows the experimental results of the single-stage single-phase inverter system, where the PV input power is suddenly changed from 1250 to 2500 W and back to 1250 W, respectively. It can be seen in Fig. 18 that the transient periods t_s are 34 and

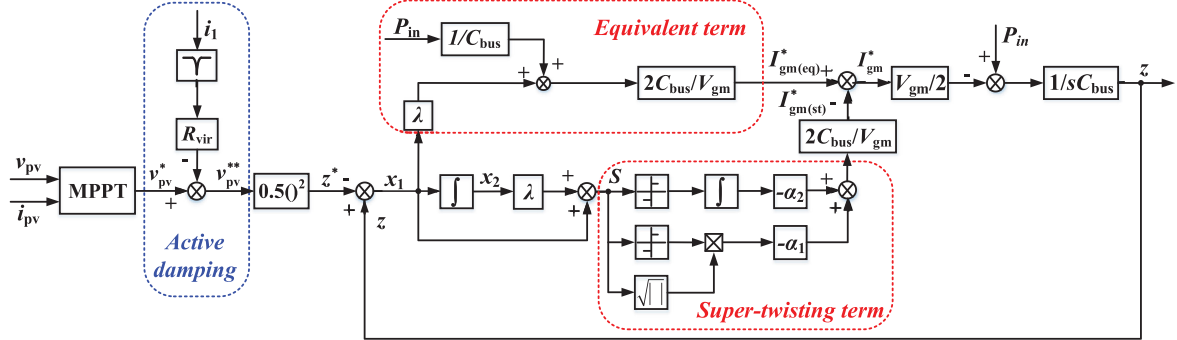


Fig. 14. Control block diagram of the dc-link voltage loop with the proposed SOSMC for single-stage single-phase grid-connected inverter.

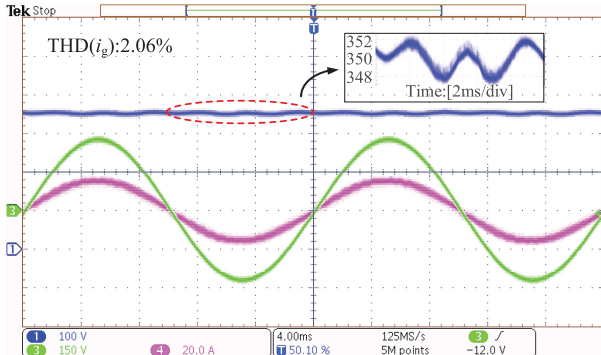


Fig. 15. Experimental results of the single-stage single-phase system under steady-state condition.

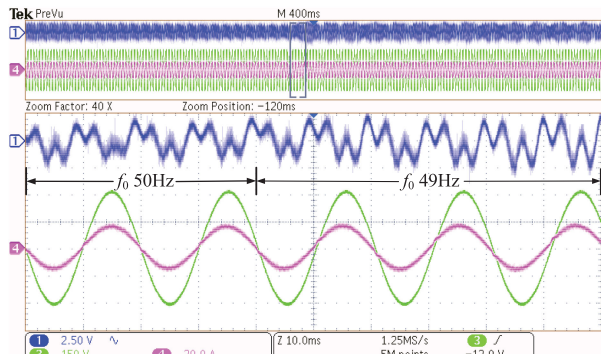


Fig. 16. Experimental waveform of dc-link voltage for a step change in grid frequency f_0 from 50 to 49 Hz.

30 ms, respectively, and the overshoots σ are 3% and 2.75%, respectively. Furthermore, to demonstrate the superior dynamic performance of the proposed method in term of MPP tracking, the P&O MPPT algorithm is added into controller. The experimental results of the system under the irradiance step change from 500 to 1000 W/m² and back to 500 W/m² are shown in Fig. 19(a) and (b), respectively. The MPPT reaches to the steady state in 1.4 and 1.5 s, respectively, with a 99.1% dynamic MPPT efficiency. From these results, it can be observed that when a transient occurs due to the environmental change, the proposed method shows a very good performance in terms of MPPT

accuracy and speed. Thus, it is very suitable for single-stage PV generation systems.

D. Sensitivity Analysis of the Proposed Controller

Sensitivity analysis is carried out to study the robustness of the SOSMC controller against a wrong knowledge of system parameters. It is known from (34) that the main capacitor C_{bus} plays an important role in determining the performance of the dc-link voltage. Therefore, the variation of the parameter C_{bus} is taken into account to determine the robustness of the proposed SOSMC. Since the capacitance tolerance of E-caps is usually $\pm 20\%$, a reduction of the parameter C_{bus} by 20% in the controller is considered in this article. Fig. 20 shows the dynamic performance of system in the case where the PV input power is suddenly changed from 1250 to 2500 W. In the test, the MPPT algorithm is disabled and the dc-link voltage is controlled as a constant. Observations in Fig. 20 confirm that the transient time and overshoot are almost the same as the results shown in Fig. 18. Similar results have been obtained for the condition where the capacitance C_{bus} is considered to increase by 20% in the controller. In all, from the abovementioned test results, it can be concluded that the proposed SOSMC scheme has high robustness and stability.

E. Comparison With Existing Methods

To further demonstrate the effectiveness of the proposed strategy, the performance of the proposed method is compared with the solution using a traditional bulky capacitor and a PI controller in the voltage loop (denoted as PI + bulky capacitor solution). For a fair comparison, the current loop is also the P+MR controller. The dc-link capacitor is 2500 μ F, and a $2f_0$ -notch filter is added into the voltage loop to mitigate the influence of $2f_0$ -ripple voltage on the grid current. Fig. 21 shows the steady-state waveforms of the dc-link voltage, grid current, and grid voltage. It can be seen in Fig. 21 that with the notch filter, the THD of the grid current is 2.64% even with the amplitude of the dc-link $2f_0$ -ripple voltage being 12 V. Although an MAF, whose window frequency is $2f_0$, is adopted in the controller to better calculate the MPP. The large ripple shifts the operating point away from the desired MPP point, which leads to a static MPPT efficiency of 98.6%. When comparing Figs. 15 and 21, it can be

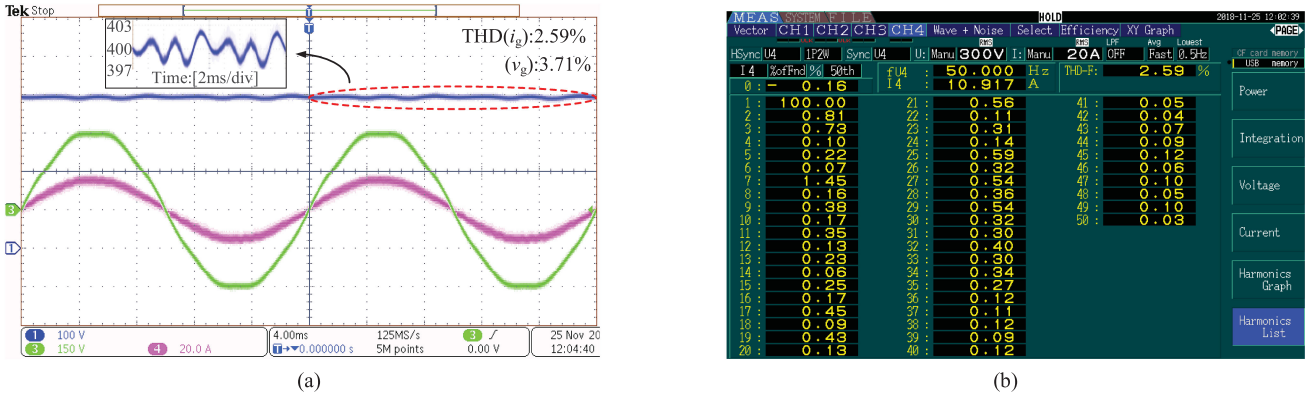


Fig. 17. Steady-state waveforms with the proposed SOSMC under a distorted grid. (a) Experimental waveform. (b) Experimental spectrum of grid current.

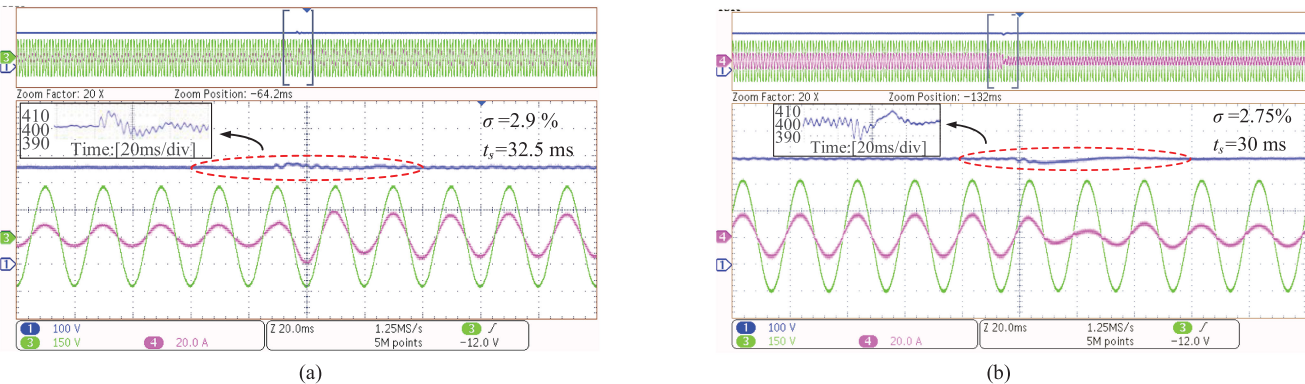


Fig. 18. Experimental results of the dynamic waveforms with the proposed SOSMC method in the PV system. (a) Waveform of v_{pv} , i_g , and v_g for a step change in P_{in} from half load to full load. (b) PV input power P_{in} from full load back to half load.

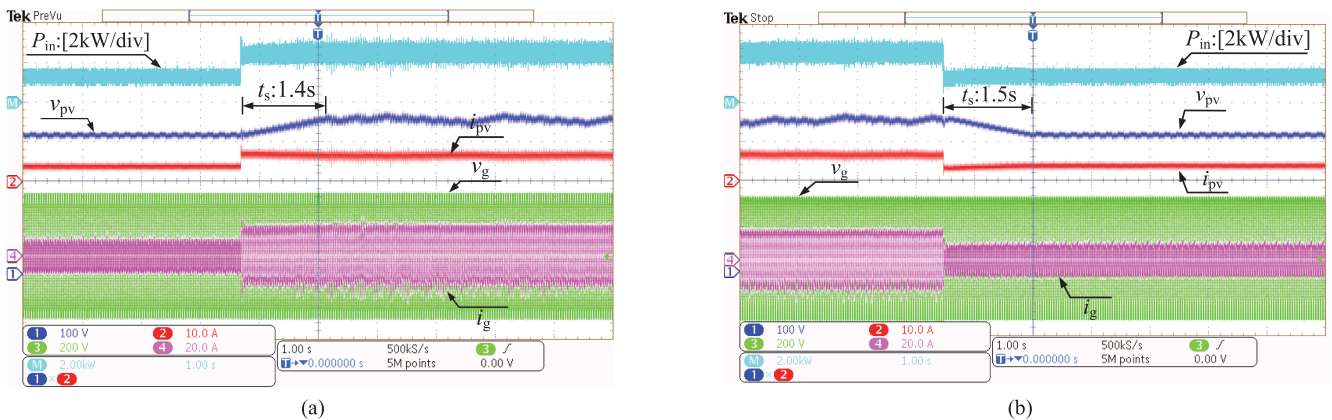


Fig. 19. MPPT performance with the proposed method in the cases of irradiance is suddenly changed from 500 to 1000 W/m^2 and back to 500 W/m^2 .

concluded that the proposed method for single-state single-phase PV system can ensure a better steady-state performance. Also, it confirms that the double-line frequency will affect the MPPT and system performance (leading to a lower efficiency and power quality).

Similar to the previous tests, the dynamic performance of the voltage loop with the conventional method is also tested,

where the MPPT algorithm is disabled, and the dc-link voltage is controlled as a constant. Fig. 22(a) and (b) shows the dynamic response of the dc-link voltage and grid current, where the PV input power is changed from 1250 to 2500 W and back to 1250 W . It is clearly shown in Fig 22 that the transient periods t_s are 110 and 120 ms with 4.4% and 5% overshoots, respectively. By comparing Figs. 18 and 22, it is known that the proposed

TABLE II
COMPARISONS OF THE PROPOSED SCHEME WITH EXISTING SCHEMES

Comparison category	PI control + capacitor [46]	Adaptive PI control + bulky capacitor [23]	PI control + bulky capacitor + feedforward dc current [28]	PI control + bulky capacitor + feedforward dc bus control loop [27]	Proposed method
Number of converter stage	Two-stage	Single-stage	Single-stage	Single-stage	Single-stage
Number of phase	Single-phase	Single-phase	Single-phase	Three-phase	Single-phase
Controller of voltage loop	PI	Adaptive PI	PI+ feedforward control	PI+ feedforward control	SOSMC
DC-link capacitor (μF)	112	1100	1100	2350	200
Input power (W)	250	500	225	2500	2500
Switching frequency f_s (kHz)	20	40	20	20	20
Filter type	L	L	L	L	L
Filter inductor (mH)	10	7	20	3.5	2
Grid current THD i_g (%)	13	4.7	11.03	2.7	2.06
DC-link ripple (V)	14.8	7.3	4.34	-	4
Transient time (ms)	75	100	184	250	34
Overshoot of dc-bus voltage σ (%)	5.6	5.5	9.3	3	3

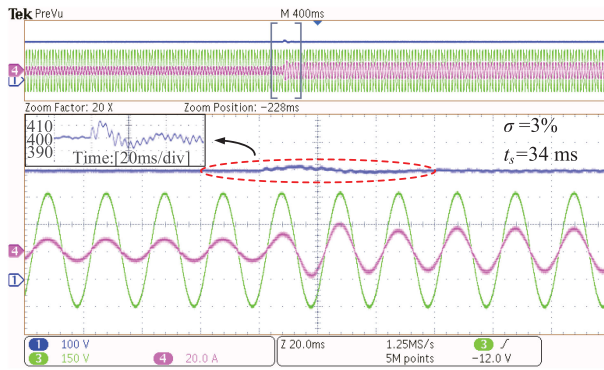


Fig. 20. Dynamic performance of the system with the proposed SOMSC in the case of parameter C_{bus} reduced by 20% in controller.

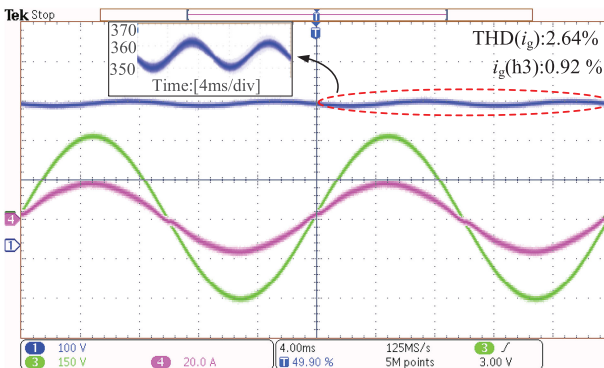


Fig. 21. Steady-state waveforms with the traditional PI + bulky capacitor method.

strategy outperforms over the conventional method in terms of dynamics (voltage fluctuation and transient time). To test the dynamic MPPT performance of the traditional method, the P&O MPPT algorithm is then activated in the controller. Fig. 23(a) and (b) shows the experimental results of the system experiencing an irradiance step change from 500 to 1000 W/m^2 and back to 500 W/m^2 , respectively. It can be observed in Fig. 23 that due to the oscillation of the dc-link voltage and the slow dynamics of the

voltage loop, the MPPT takes more than 5 s to reach the steady state with a dynamic MPPT efficiency of 97.4%. Compared with the performance in Fig. 19, it is clear that the proposed method is more suitable for single-stage PV systems, which ensures the MPPT performance under various conditions.

Moreover, Table II compares the proposed control scheme with the existing schemes [23], [27], [28], [46] in terms of steady-state and dynamic performances. It is worth noting that when compared with the scheme introduced in [23] and [46], although the transient periods with a small dc-link capacitor is reduced, the THD of the grid current is unacceptable even with a 10-mH ac filter inductor. This is because the small capacitor leads to a large dc-link $2f_0$ -ripple voltage, which increases the third-order harmonics appearing in the grid current. As it can be seen in [27], with a feedforward control method, the setting time and overshoot have been substantially reduced even with a bulky capacitor. However, as mentioned previously, such a feedforward path increases the coupling between dc and ac sides, which will lead to large harmonics at the output reference current. In worst cases, this may even challenge the stability of the system. This conclusion can be confirmed by comparing [23] and [28]. In [28], although the dc-side current is estimated by a state observer and fed forward, the THD of the grid current is far higher than that obtained in [23]. A close inspection of Table II shows that the proposed strategy outperforms over the benchmarked solutions in terms of the steady-state (a small THD of the grid current) and dynamic (fast response and small overshoots) performances.

To exhibit the performance of the proposed method, another detailed comparison is carried out among the proposed method, conventional bulky capacitor method, and APD scheme [47] in terms of volume, cost, and efficiency. The results are shown in Table III, where the cost analysis is done referring to [48] and Mouser [49] with the minimum ordering quantity (MOQ) being 10 000. In Table III, the system cost of the conventional method and the proposed method is calculated in the case the HERIC inverter is adopted. However, it should be pointed out that the proposed method can also be applied to the H-bridge inverter. In addition, compared with the conventional bulky capacitor method, the proposed strategy requires an additional

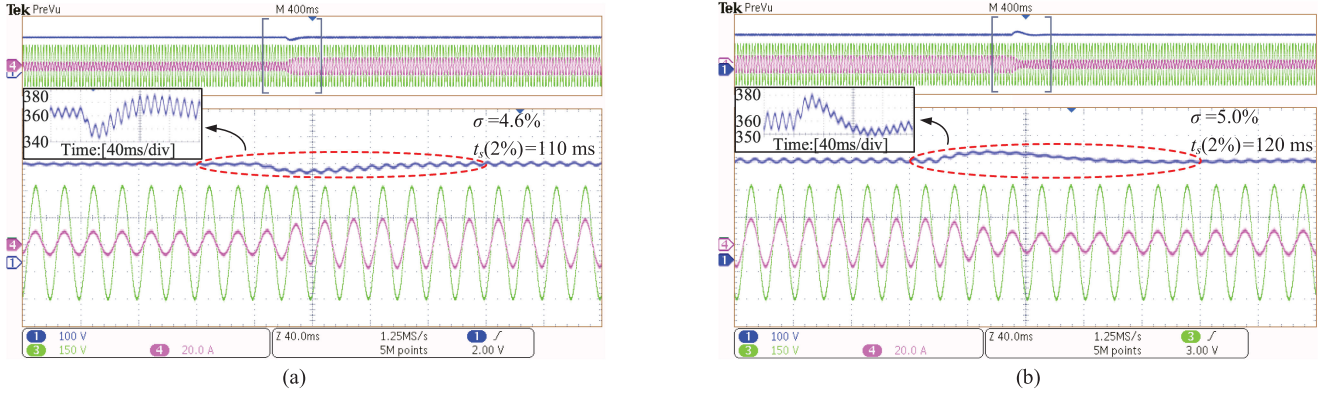


Fig. 22. Dynamic responses of the dc-link voltage and grid current with PV input power P_{in} is suddenly changed. (a) Half load to full load. (b) Back to half load.

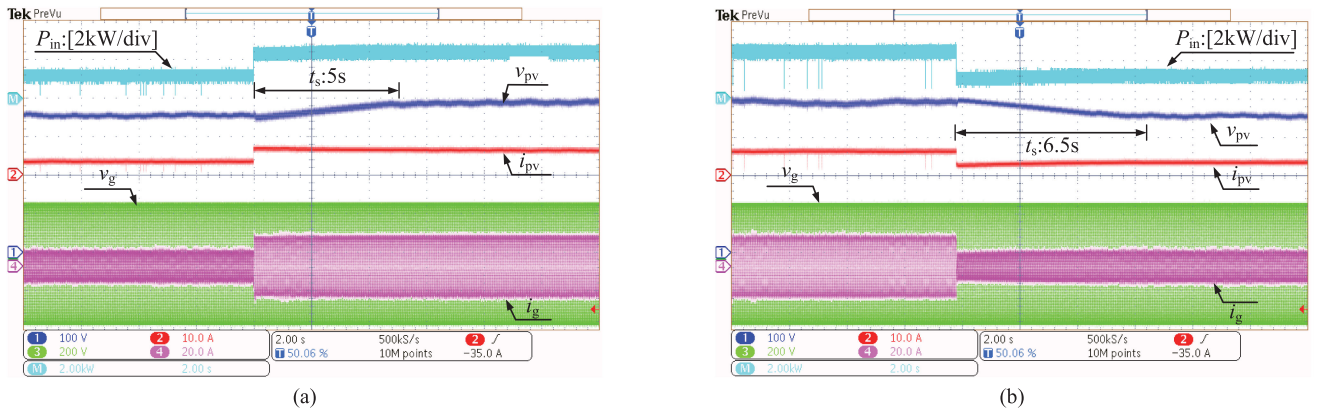


Fig. 23. MPPT performance with the PI+ bulky capacitor method under the condition of irradiance is suddenly changed from 500 to 1000 W/m² and back to 500 W/m².

TABLE III
VOLUME, COST, AND EFFICIENCY COMPARISONS OF THE THREE METHODS

Method	Devices for converter and active decoupling circuit, Number	Rated Power (kW)	Volume ¹⁾ (cm ³)	Total Cost ²⁾ (€)	Peak conversion Efficiency (%)
Traditional method	Si (IKW30N65EL5), 6	2.5	452.4	98.6	97.78
Proposed method	Si (IKW30N65EL5), 6	2.5	365.1	81.8	97.47
APD [47]	GaN (GS66508P), 6	2	108.3	148.1	98

¹⁾ only the passive components of decoupling circuit is considered; ²⁾ both the decoupling circuit and converter are considered

sensor to measure the current i_1 to achieve active damping. Notably, as analyzed above, since the current i_1 is sinusoidal with a frequency of $2f_0$, it is measured by a cheap current transformer rather than an expensive Hall sensor. In all, according to Table III, the proposed method achieved the lowest cost, whereas the efficiency is still comparable with the traditional and the APD methods. In terms of volume, it achieves a moderate performance. The comparison is further presented in Fig. 24. Although the system maximum conversion efficiency of the proposed method is slightly lower, 0.31%, than that of the traditional method, the static and dynamic MPPT efficiencies

are increased by 0.9% and 1.7%, respectively. Thus, the total system generation efficiency of the proposed method still has an advantage. Thanks to the wide-bandgap gallium nitride (GaN) field-effect transistors, the smallest volume and 98% system conversion efficiency are achieved with APD schemes, but it comes at a high cost. Although the cost of the APD scheme can be reduced when silicon devices are used to replace the GaN devices, the overall efficiency will decrease by approximately 2% than that of the conventional method [50]. Since low cost and high efficiency are of importance in PV generation systems, the passive decoupling method may be preferred in PV applications.

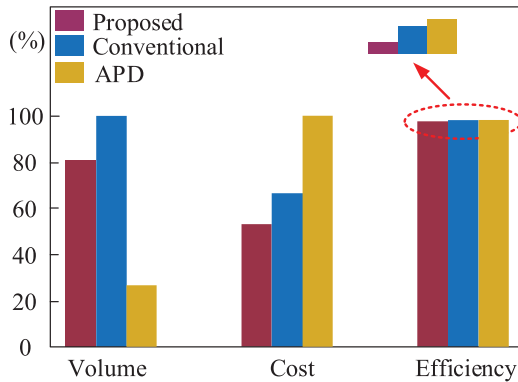


Fig. 24. Volume, cost, and conversion efficiency of the system with the three decoupling method.

VI. CONCLUSION

In this article, a control and design method to enhance the MPPT accuracy and speed was proposed for single-stage single-phase PV grid-connected inverters. The proposed method can be divided into two parts, a passive *LC* decoupling method and a robust control strategy. With the passive *LC* decoupling circuit, the $2f_0$ -voltage ripple is suppressed, where a small dc-link capacitor can be used. Thus, the MPPT accuracy and the dynamics of the entire system are improved. To design the parameters of *LC* decoupling circuit, a PSO algorithm was adopted to realize optimal parameters design. It is worth noting that the resonance between the passive *LC* branch and main capacitor is damped by introducing a virtual resistance. Consequently, the system stability is improved without additional losses. Furthermore, a robust SOSMC was proposed to improve the steady-state and dynamic performances of the dc-link voltage, which further increases the MPPT accuracy and speed. The impact of system parameter uncertainties on the controller was also studied, and the system stability was proved by the Lyapunov approach. Various experimental results and comparisons have been provided, which demonstrates that the proposed method achieves good MPPT performances both in steady-state and dynamics under various conditions. Hence, it is suitable for single-stage single-phase grid-connected PV systems.

REFERENCES

- B. Liu *et al.*, "Input current ripple and grid current harmonics restraint approach for single-phase inverter under battery input condition in residential photovoltaic/battery systems," *IEEE Trans. Sustain. Energy*, vol. 9, no. 4, pp. 1957–1968, Oct. 2018.
- B. Guo *et al.*, "A robust second-order sliding mode control for single-phase photovoltaic grid-connected voltage source inverter," *IEEE Access*, vol. 7, pp. 53202–53212, Apr. 2019.
- J. Hu, J. Zhu, and D. G. "Model predictive control of grid-connected inverters for PV systems with flexible power regulation and switching frequency reduction," *IEEE Trans. Ind. Appl.*, vol. 51, no. 1, pp. 587–594, Jan. 2015.
- M. Calais, J. Myrzik, T. Spooner, and V. Agelidis, "Inverters for single-phase grid connected photovoltaic systems: An overview," in *Proc. IEEE Power Electron. Spec. Conf.*, 2002, pp. 1995–2000.
- M. Fortunato, A. Giustiniani, G. Petrone, G. Spagnuolo, and M. Vitelli, "Maximum power point tracking in a one cycle controlled single stage photovoltaic inverter," *IEEE Trans. Ind. Electron.*, vol. 55, no. 7, pp. 2864–2693, Jul. 2008.
- E. S. Sreeraj, K. Chatterjee and S. Bandyopadhyay, "One-cycle-controlled single-stage single-phase voltage-sensorless grid-connected PV system," *IEEE Trans. Ind. Electron.*, vol. 60, no. 3, pp. 1216–1224, Mar. 2013.
- F. Chan and H. Calleja, "Reliability estimation of three single-phase topologies in grid-connected PV systems," *IEEE Trans. Ind. Electron.*, vol. 58, no. 7, pp. 2683–2689, Jul. 2011.
- B. N. Alajmi, K. H. Ahmed, G. P. Adam, and B. W. Williams, "Single-phase single-stage transformerless grid-connected PV system," *IEEE Trans. Power. Electron.*, vol. 28, no. 6, pp. 2664–2676, Jun. 2013.
- V. M. Lyer and V. John, "Low-frequency DC bus ripple cancellation in single phase pulse-width modulation inverters," *IET Power. Electron.*, vol. 8, no. 4, pp. 497–506, Apr. 2015.
- X. G. Fu and S. H. Li, "Control of single-phase grid-connected converters with LCL filters using recurrent neural network and conventional control methods," *IEEE Trans. Power. Electron.*, vol. 31, no. 7, pp. 5354–5364, Jul. 2016.
- Y. Tang, F. Blaabjerg, P. C. Loh, C. Jin and P. Wang, "Decoupling of fluctuating power in single-phase systems through a symmetrical half-bridge circuit," *IEEE Trans. Power. Electron.*, vol. 30, no. 4, pp. 1855–1865, Apr. 2015.
- J. C. Das, "Passive filters-potentialities and limitations," *IEEE Trans. Ind. Appl.*, vol. 40, no. 1, pp. 232–241, Jan. 2004.
- S. Harb, M. Mirjafari, and R. S. Balog, "Ripple-port module-integrated inverter for grid-connected PV applications," *IEEE Trans. Ind. Appl.*, vol. 49, no. 6, pp. 2692–2698, Nov. 2013.
- Y. Sun, Y. L. Liu, M. Su, W. J. Xiong, and J. Yang, "Review of active power decoupling topologies in single-phase systems," *IEEE Trans. Power. Electron.*, vol. 31, no. 7, pp. 4778–4794, Jul. 2016.
- Y. Sun, Y. L. Liu, M. Su, X. Li, and J. Yang, "Active power decoupling method for single-phase current-source rectifier with no additional active switches," *IEEE Trans. Power. Electron.*, vol. 31, no. 8, pp. 5644–5654, Aug. 2016.
- R. Wang *et al.*, "A high power density single-phase PWM rectifier with active ripple energy storage," *IEEE Trans. Power. Electron.*, vol. 26, no. 5, pp. 1430–1443, May 2011.
- S. Q. Kan, X. B. Ruan, H. Dang, L. Zhang, and X. Huang, "Second harmonic current reduction in front-end DC–DC converter for two-stage single-phase photovoltaic grid-connected inverter," *IEEE Trans. Power. Electron.*, vol. 34, no. 7, pp. 6399–6410, Jul. 2011.
- G. Zhu, X. B. Ruan, L. Zhang, and X. Wang, "On the reduction of second harmonic current and improvement of dynamic response for two-stage single-phase inverter," *IEEE Trans. Power. Electron.*, vol. 30, no. 2, pp. 1028–1041, Feb. 2015.
- Y. J. Shi, B. Liu, and S. Duan, "Low-frequency input current ripple reduction based on load current feed forward in a two-stage single phase inverter," *IEEE Trans. Power. Electron.*, vol. 31, no. 11, pp. 7972–7985, Dec. 2016.
- D. H. Hwang, J. Y. Lee, and Y. Cho, "Single-phase single-stage dual-buck photovoltaic inverter with active power decoupling strategy," *Renewable Energy*, vol. 126, pp. 454–464, 2018.
- Y. Yu, Q. Zhang, B. Liang, and S. Cui, "single-phase Z-source inverter: Analysis and low-frequency harmonics elimination pulse width modulation," in *Proc. IEEE Energy Convers. Congr. Expo.*, Sep. 17–22, 2011, pp. 2260–2267.
- Y. Zhou, H. B. Li, and H. Li, "A single-phase PV quasi-Z-source inverter with reduced capacitance using modified modulation and double-frequency ripple suppression control," *IEEE Trans. Power. Electron.*, vol. 31, no. 3, pp. 2166–2173, Mar. 2016.
- M. Merai, M. W. Naouar, I. S. Belkhodja, and E. Monmasson, "An adaptive PI controller design for DC-link voltage control of single-phase grid-connected converters," *IEEE Trans. Ind. Electron.*, vol. 66, no. 8, pp. 6241–6249, Aug. 2016.
- M. C. Kisacikoglu, M. Kesler, and L. M. Tolbert, "Single-phase on-board bidirectional PEV charger for V2G reactive power operation," *IEEE Trans. Smart Grid*, vol. 6, no. 2, pp. 767–775, Mar. 2015.
- Y. J. Shi, B. Y. Liu, and S. X. Duan, "Modeling, control and performance analysis of a single-stage single-phase inverter with reduced low-frequency input current ripple," *IET Power. Electron.*, vol. 11, no. 6, pp. 1074–1082, May 2018.
- S. A. Khajehoddin, M. Karimi-Ghartemani, P. K. Jain, and A. Bakhshai, "DC-bus design and control for a single-phase grid-connected renewable converter with a small energy storage component," *IEEE Trans. Power. Electron.*, vol. 28, no. 7, pp. 3245–3254, Jul. 2013.

- [27] L. B. G. Campanbol, S. A. O. da Silva, A. A. de Oliveira and V. D. Bacon, "Single-stage three-phase grid-tied PV system with universal filtering capability applied to DG systems and AC microgrids," *IEEE Trans. Power Electron.*, vol. 32, no. 12, pp. 9131–9142, Dec. 2017.
- [28] N. Baazoug, M. W. Naouar, and E. Monmasson, "Design of an adaptive feed-forward control scheme for the DC bus voltage control of single phase grid connected converters," in *Proc. IEEE Int. Ind. Technol.*, Lyon, France, 2018, pp. 682–687.
- [29] Z. T. Tang *et al.*, "A hybrid UP-PWM scheme for HERIC inverter to improve power quality and efficiency," *IEEE Trans. Power Electron.*, vol. 34, no. 5, pp. 4292–4303, May 2019.
- [30] C. W. T. Mclyman, *Transformer And Inductor Design Handbook*, 4th ed, Boca Raton, FL, USA: CRC Press, 2011.
- [31] D. Zhao, W. Liu, K. Shen, G. Zhao and X. Wang, "Multi-objective optimal design of passive power filter for aircraft starter/generator system application," *J. Eng.*, vol. 2018, no. 13, pp. 636–641, 2018.
- [32] Y. L. Xia, J. Roy, and R. Ayynaar, "A capacitance minimized, doubly grounded transformerless photovoltaic inverter with inherent active-power decoupling," *IEEE Trans. Power Electron.*, vol. 32, no. 7, pp. 5188–5201, Jul. 2017.
- [33] Y. Liu, M. Huang, H. Wang, X. M. Zha, J. W. Gong, and J. J. Sun, "Reliability-oriented optimization of the LC filter in a buck DC–DC converter" *IEEE Trans. Power Electron.*, vol. 32, no. 8, pp. 6323–6337, Aug. 2017.
- [34] Datasheet: EPCOS (TDK) Electrolytic Capacitors, 2019. [Online]. Available: <https://www.mouser.cn/datasheet/2/400/B43231-1206869.pdf>.
- [35] Datasheet: Nichicon Electrolytic Capacitors, 2019. [Online]. Available: <https://www.mouser.cn/datasheet/2/293/e-vz-6403.pdf>.
- [36] Datasheet: United Chemi-Con (UCC) Electrolytic Capacitors, 2019. [Online]. Available: <https://www.mouser.cn/datasheet/2/420/United-Chemi-Con-346755.pdf>.
- [37] B. Seguin, J. P. Gosse, A. Sylvestre, P. Fouassier, and J. P. Ferrieux "Calorimetric apparatus for measurement of power losses in capacitors," in *Proc. Instrum. Meas. Technol. Conf.*, 1998, pp. 602–607.
- [38] L. Jiang, Y. Sun, M. Su, H. Wang, and H. B. Dan, "Optimized operation of dual-active-bridge DC–DC converters in the soft-switching area with triple-phase-shift control at light load," *J. Power Electron.*, vol. 18, no. 1, pp. 45–55, Jan. 2018.
- [39] N. He, D. Xu and L. Huang, "The application of particle swarm optimization to passive and hybrid active power filter design," *IEEE Trans. Ind. Electron.*, vol. 56, no. 8, pp. 2841–2851, Aug. 2009.
- [40] S. Taghizadeh, M. J. Hossain, J. W. Lu, and M. Karimi-Ghartemani, "An enhanced DC-bus voltage control loop for single-phase grid-connected DC/AC converters," *IEEE Trans. Power. Electron.*, vol. 34, no. 6, pp. 5819–5829, Jun. 2019.
- [41] M. Vasiladiotis, and A. Rufer, "Dynamic analysis and state feedback voltage control of single-phase active rectifiers with DC-link resonant filters," *IEEE Trans. Power. Electron.*, vol. 29, no. 10, pp. 5620–5633, Oct. 2014.
- [42] T. Ye, N. Y. Dai, C. S. Lam, M. C. Wong, and J. M. Guerrero, "Analysis, design, and implementation of a quasi-proportional-resonant controller for a multifunctional capacitive-coupling grid-connected inverter," *IEEE Trans. Ind. Appl.*, vol. 52, no. 5, pp. 4269–4280, Sep. 2016.
- [43] A. Levant, "Sliding order and sliding accuracy in sliding mode control," *Int. J. Control.*, vol. 58, no. 6, pp. 1247–1263, 1993.
- [44] J. A. Moreno, and M. Osorio, "Strict Lyapunov functions for the super-twisting algorithm," *IEEE Trans. Autom. Control.*, vol. 57, no. 4, pp. 1035–1040, Apr. 2012.
- [45] L. Fridman, J. A. Moreno, and R. Iriarte, *Sliding Modes After the First Decade of the 21st Century: State of the Art*. New York, NY, USA: Springer-Verlag, Sep. 2011.
- [46] M. K. Ghartemani, S. A. Khajehoddin, P.K. Jain, and A. Bakhshai, "A systematic approach to DC-bus control design in single-phase grid-connected renewable converters," *IEEE Trans. Power. Electron.*, vol. 28, no. 7, pp. 3158–3266, Jul. 2013.
- [47] A. S. Morsy and P. N. Enjeti, "Comparison of active power decoupling methods for high-power-density single-phase inverters using wide-bandgap FETs for Google little box challenge," *IEEE J. Emerg. Sel. Topics Power Electron.*, vol. 4, no. 3, pp. 790–798, Sep. 2016.
- [48] R. M. Burkart, and J. Kolar, "Component cost model for multi-objective optimization of switched-mode power electronics," in *Proc. IEEE Energy Convers. Congr. Expo.*, 2013, pp. 2139–2146.
- [49] 2019. [Online]. Available: <http://www.mouser.cn>
- [50] I. Serban, "Power decoupling method for single-phase H-bridge inverters with no additional power electronics," *IEEE Trans. Ind. Electron.*, vol. 62, no. 8, pp. 4805–4813, Aug. 2015.



Bin Guo was born in Hubei, China, in 1992. He received the B.S. degree in electrical engineering from Beihua University, Jilin, China, in 2015. He is currently working toward the Ph.D. degree in the electrical engineering at Central South University, Changsha, China.

His current research interests include modeling and control of power electronics and its application in renewable energy and energy storage systems.



Mei Su was born in Hunan, China, in 1967. She received the B.S., M.S., and Ph.D. degrees from Central South University, Changsha, China, in 1989, 1992 and 2005, respectively.

Since 2006, she has been a Full Professor with the School of Automation, Central South University. Her research interests include matrix converter, adjustable speed drives, photovoltaic system, and wind conversion system.

Dr. Su is currently an Associate Editor for the IEEE TRANSACTIONS ON POWER ELECTRONICS.



Yao Sun (Member, IEEE) was born in Hunan, China, in 1981. He received the B.S., M.S., and Ph.D. degrees from Central South University, Changsha, China, in 2004, 2007, and 2010, respectively.

Since 2013, he has been a Full Professor with the School of Automation, Central South University. His research interests include matrix converter, micro-grid, and wind energy conversion systems.



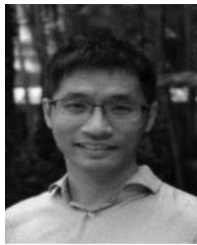
Hui Wang received the B.S., M.S., and Ph.D. degrees from Central South University, Changsha, China, in 2008, 2011, and 2014, respectively.

He is currently an Associate Professor with the School of Automation, Central South University. His research interests include matrix converters, dc/dc converters, and solid-state transformers.



Bin Liu received the Ph.D. degree from the School of Information Science and Engineering, Central South University, Changsha, China, in 2014.

Since 2015, he has been an Associate Professor with the School of Electrical Engineering, Guangxi University. His research interests include the general area of power electronics and energy conversion, with particular emphasis on converter topologies, modeling, and control.



Xin Zhang (Senior Member, IEEE) received the Ph.D. degree in automatic control and systems engineering from the University of Sheffield, U.K., in 2016, and the Ph.D. degree in electronic and electrical engineering from the Nanjing University of Aeronautics & Astronautics, China, in 2014.

He is currently an Assistant Professor of power engineering with the School of Electrical and Electronic Engineering, Nanyang Technological University. From January 2017 to December 2016, he was a Postdoctoral Research Fellow with the City University of Hong Kong. From February 2014 to December 2016, he was a Research Associate with the University of Sheffield. His research interests include power electronics, power system, and advanced control theory, together with their applications in various sectors.

Dr. Zhang was the recipient of highly prestigious Chinese National Award for Outstanding Students Abroad in 2016. He is the Associated Editor for the IEEE TRANSACTIONS ON INDUSTRIAL ELECTRONICS/IEEE JOURNAL OF EMERGING AND SELECTED TOPICS IN POWER ELECTRONICS/IEEE OPEN JOURNAL OF ANTENNAS AND PROPAGATION, IEEE ACCESS, and the *IET Power Electronics*.



Yongheng Yang (Senior Member, IEEE) received the B.Eng. degree in electrical engineering and automation from Northwestern Polytechnical University, Shaanxi, China, in 2009, and the Ph.D. degree in electrical engineering from Aalborg University, Aalborg, Denmark, in 2014.

He was a Postgraduate Student with Southeast University, China, from 2009 to 2011. In 2013, he spent three months as a Visiting Scholar with Texas A&M University, USA. He is currently an Associate Professor with the Department of Energy Technology, Aalborg University, where he also serves as the Vice Program Leader for the research program on photovoltaic systems. His current research include the integration of grid-friendly photovoltaic systems with an emphasis on the power electronics converter design, control, and reliability.

Dr. Yang is the Chair of the IEEE Denmark Section. He serves as an Associate Editor for several prestigious journals, including the IEEE TRANSACTIONS ON INDUSTRIAL ELECTRONICS, the IEEE TRANSACTIONS ON POWER ELECTRONICS, and the IEEE Industry Applications Society Publications. He is a Subject Editor of the IET Renewable Power Generation for Solar Photovoltaic Systems, including the Maximum Power Point Tracking. He was the recipient of the 2018 IET Renewable Power Generation Premium Award and was an Outstanding Reviewer for the IEEE TRANSACTIONS ON POWER ELECTRONICS in 2018.



Josep Pou (Fellow, IEEE) received the B.S., M.S., and Ph.D. degrees in electrical engineering from the Technical University of Catalonia (UPC)-Barcelona Tech, in 1989, 1996, and 2002, respectively.

In 1990, he joined as an Assistant Professor with the Faculty of UPC, where he became an Associate Professor in 1993. From February 2013 to August 2016, he was a Professor with the University of New South Wales (UNSW), Sydney, Australia. He is currently a Professor with the Nanyang Technological University (NTU), Singapore, where he is also the Program Director of Power Electronics at the Energy Research Institute at NTU (ERI@N) and the Co-Director of the Rolls-Royce at NTU Corporate Lab. From February 2001 to January 2002, and February 2005 to January 2006, he was a Researcher with the Center for Power Electronics Systems, Virginia Tech, Blacksburg, VA, USA. From 2012 to 2013, he was a Visiting Professor with the Australian Energy Research Institute, UNSW, Sydney. He has authored more than 320 published technical papers and has been involved in several industrial projects and educational programs in the fields of power electronics and systems. His research interests include modulation and control of power converters, multilevel converters, renewable energy, energy storage, power quality, HVdc transmission systems, and more-electrical aircraft and vessels.

Dr. Pou is the Co-Editor-in-Chief of the IEEE TRANSACTIONS ON INDUSTRIAL ELECTRONICS and an Associate Editor for the IEEE JOURNAL OF EMERGING AND SELECTED TOPICS IN POWER ELECTRONICS. He was the recipient of the 2018 IEEE Bimal Bose Award for Industrial Electronics Applications in Energy Systems.



Pooya Davari (Senior Member, IEEE) received the B.Sc. and M.Sc. degrees in electronic engineering in 2004 and 2008, respectively, and the Ph.D. degree in power electronics from the Queensland University of Technology (QUT), Australia, in 2013.

From 2005 to 2010, he was involved in several electronics and power electronics projects as a Development Engineer. From 2013 to 2014, he was a Lecturer with QUT. In 2014, as a Postdoctoral Researcher he joined Aalborg University, where he is currently an Associate Professor. He has been focusing on electromagnetic interference, power quality and harmonic mitigation analysis and control in power electronic systems. He has authored/coauthored more than 120 technical papers.

Dr. Davari was the recipient of a research grant from the Danish Council of Independent Research (DFF-FTP) in 2016. He served as a Guest Associate Editor for the *IET Journal of Power Electronics*, IEEE ACCESS, *Journal of Electronics*, and *Journal of Applied Sciences*. He is an Associate Editor for the *Journal of Power Electronics* and *IET Electronics* and an editorial board member of *EPE Journal* and *Journal of Applied Sciences*. He is a member of the International Scientific Committee of EPE (ECCE Europe) and a member of Joint Working Group six and Working Group eight at the IEC standardization TC77A.